





Multifilter Time-series Observations of Eleven Blue Short-period ATLAS Variable Stars

C. Koen¹ , V. Schaffenroth², and A. Kniazev^{3,4,5} ¹ Department of Statistics, University of the Western Cape, Private Bag X17, Bellville, 7535 Cape, South Africa² Institut für Physik und Astronomie, Universität Potsdam, Karl-Liebknecht-Strasse 24/25, Germany³ South African Astronomical Observatory, P.O. Box 9, Observatory, 7935 Cape, South Africa⁴ Southern African Large Telescope, P.O. Box 9, Observatory, 7935 Cape, South Africa⁵ Special Astrophysical Observatory, Niznij Arkhyz, Karachai-Circassia, 369167, Russia

Received 2022 December 30; revised 2023 February 2; accepted 2023 February 2; published 2023 March 2

Abstract

Eleven periodic variable stars were observed photometrically through two to four filters from the set $UBVR_CI_C$. Phase-folded data for each star cover full cycles of variation. Spectral energy distributions, based on absolute photometry extracted from the literature, are used to inform models of the stars. The stars include four eclipsing systems with hot subdwarfs of spectral type O or B (sdO/B). Periods are in the range 1.8–2.2 hr. Four reflection-effect binaries, with amplitudes as large as 0.5 mag in the R_C filter were observed; periods range from 1.6 to 2.4 hr. In two of these latter systems, the primary stars are also sdB stars, while two have white-dwarf components. In all eight of these binaries the companion stars are probably M dwarfs. The remaining three stars are pulsators: one large-amplitude δ Scuti star previously misclassified as an eclipsing system; one field SX Phe star near the Galactic plane; and one multiperiodic high-luminosity star of unknown type. The amplitude is usually a strong function of the wavelength in pulsating stars, but this is not the case for the high-luminosity variable. One possible explanation is that the luminous star has a pulsating companion. The SX Phe and high-luminosity star are both heavily reddened ($A_V > 5$ mag).

Unified Astronomy Thesaurus concepts: Subdwarf stars (2054); Close binary stars (254); Variable stars (1761)

Supporting material: figure sets

1. Introduction

As pointed out by Koen (2019), the Asteroid Terrestrial-impact Last Alert System (ATLAS) variable star catalog (Heinze et al. 2018) is an important resource in the search for binary stars with very short periods (here meaning $P < 0.2$ days). In particular, because of the large number ($> 300,000$) of stars in the ATLAS catalog, it is not difficult to find candidates with color indices characteristic of either very high or very low temperatures. Arguments were presented in Koen (2019) as to why very hot and very cool short-period binaries are of special interest—in short, ascertaining the physical properties of such systems helps to understand the binary evolution of stars with extreme temperatures. The point is discussed at some length by Schaffenroth et al. (2018) for the case of hot subdwarf stars in short-period binary systems. These systems are thought to be the products of common envelope evolution during which the subdwarf star loses considerable mass while passing through a red-giant phase. In this context, the nature of the companion star is of interest in order to test the statistics of binary population models (e.g., Han et al. 2002, 2003).

Here we present photometry of 11 stars from an ongoing observational program devoted to further study of ATLAS binaries. The target stars (see Table 1) were all selected on the basis of their $g-i$ and $r-z$ color indices, and their accessibility from the observing site at 34° South. Eight of the stars are sufficiently blue ($g-i < -0.4$, $r-z < -0.4$) for them to have entries in either a catalog of hot subdwarf candidates (Geier et al. 2019) and/or a catalog of white-dwarf

candidates (Gentile Fusillo et al. 2019). The exceptions are, first, ATL 1843+0226 and ATL 1853+0339, which were actually selected for their short periods and extremely red colors ($g-i > 2.2$, $r-z > 1.5$) as candidate ultrashort-period ($P < 0.2$ days) late-type binary stars. Analysis however revealed that these two objects are heavily reddened blue stars. The other exception is ATL 0843-1159, which is not quite as blue as the hot subdwarf and white-dwarf candidates, though evidently still quite hot ($g-i = -0.25$, $r-z = -0.32$). The star is classified as a contact binary with a period of 0.115 day (2.8 hr) by Heinze et al. (2018); the combination of this variability type and color is unusual.

Table 1 summarizes some basic information about the target stars. The abbreviated names in the second column will be used in the rest of the paper. None of these objects have received individual attention in the literature, i.e., all published information about them is part of large studies of many stars. The periods of the stars in Table 1 are not all given to the same accuracy. This is because some periods were determined from Catalina Sky Survey (CSS; Drake et al. 2014) photometry: the time baseline of the CSS is longer, and hence period determinations from those data are potentially more accurate. Note that for ATL 0843-1159 and ATL 1843+0226 the correct periods are half the ATLAS catalog values. In the case of ATL 1544-1816, the periodogram maxima occur at 14.2397, 16.2447, and 15.2423 day^{-1} for the ATLAS c , ATLAS o , and CSS data, respectively, while the ATLAS catalog period is 0.140453 d, corresponding to a frequency of $14.2396/2 \text{ day}^{-1}$. The new observations discussed in this paper confirm that the period derived from the CSS data is the correct alias.

The ATLAS survey uses two filters— c (“cyan”) and o (“orange”), with respective ranges of 420–650 and 560–820 nm. Each star was observed ~ 100 times through

Table 1
Summary of Some Properties of the Stars Discussed in this Paper

Catalog name	Short Name	Period (day)	g (mag)	$g - i$ (mag)	$r - z$ (mag)	$p(\sigma_p)$ (mas)	Type
ATO J079.5290-23.1459	ATL 0518-2308	0.0911720	15.704	-0.707	-0.615	0.4162(0.0372)	sdB
ATO J084.4719-00.8240	ATL 0537-0049	0.0755278	15.118	-0.422	-0.451	0.8031(0.0322)	sdB
ATO J109.7403+07.6537	ATL 0718+0739	0.084461	15.100	-0.785	-0.532	0.5247(0.0476)	sdO/B
ATO J129.0543-08.0399	ATL 0836-0802	0.0888684	15.143	-0.751	-0.605	0.5070(0.0495)	sdB
ATO J130.7753-11.9973	ATL 0843-1159	0.0575772h	14.302	-0.250	-0.323	0.4512(0.0187)	A-F
ATO J236.1079-18.2809	ATL 1544-1816	0.0656070h	17.428	-0.565	-0.546	0.9952(0.1121)	WD
ATO J267.1557+09.1634	ATL 1748+0909	0.096456	16.579	-0.515	-0.538	0.4825(0.0571)	sdB
ATO J280.9765+02.4482	ATL 1843+0226	0.039549h	19.374	2.998	1.788	0.5773(0.0699)	A-F
ATO J283.3857+03.6586	ATL 1853+0339	0.118055	18.759	3.696	2.373	0.3624(0.0456)	B-A
ATO J300.8707+08.6464	ATL 2003+0838	0.098602	14.388	-0.922	-0.658	2.5890(0.0421)	WD
ATO J307.2199+06.1675	ATL 2028+0610	0.094216	14.711	-0.538	-0.495	0.8981(0.0340)	sdO/B

Note. Periods from Catalina Sky Survey observations are quoted when these are available; otherwise periods are from the ATLAS catalog. Periods marked with an “h” are half the ATLAS period. The magnitudes and colors are from the “Panoramic Survey Telescope and Rapid Response System” (Pan-STARRS) survey. The penultimate column gives the Gaia Early Data Release 3 parallax (Gaia Collaboration 2021) and its error. For the eight bluest stars, the last column indicates whether the star is in the Geier et al. (2019) catalog of hot subdwarf stars and/or the Gentile Fusillo et al. (2019) catalog of white-dwarf (WD) candidates. For the remaining three stars, crudely estimated spectral types were obtained by fitting spectral energy distributions to published photometry—see Section 6 for details.

each filter, with measurements spread over time periods of 1.5–1.9 yr. The phase-folded ATLAS light curves are presented in the Appendix A figure set. Phased CSS light curves are included for stars observed by that survey.

The acquisition of new time-series photometry of the stars is described in the next section of the paper. The subsequent three sections deal with our binary modeling approach and its application to eclipsing and noneclipsing systems. Section 6 is devoted to the properties of three pulsating stars, followed by a brief concluding section.

2. SAAO Photometry

All observations were made with the 1 m telescope of the South African Astronomical Observatory (SAAO) situated near Sutherland, South Africa. Two CCD cameras were used—STE4 (5.28×5.28 arcmin² field of view; cryogenically cooled) and SHOC (2.85×2.85 arcmin² field of view; thermoelectrically cooled to -50°C). Both camera chips have 1024×1024 pixels and were operated in the 2×2 prebinning mode. The readout time for the STE4 camera is ~ 20 s, but SHOC is operated in frame-transfer mode, giving essentially instantaneous readout. Typically, various combinations of the Johnson UBV and Cousins $R_C I_C$ filters were used contemporaneously. (Below, the subscripts on R_C and I_C will be dropped for convenience). The exposure times were tailored to the specific stars and atmospheric conditions.

A slightly modified version of the DOPHOT CCD reduction program (Schechter et al. 1993) was used. Photometry from fitting point-spread functions is used throughout, as the noise properties were found to be better than results from aperture photometry. All photometry was differentially corrected with respect to nonvariable stars (light curves scatter typically 3–7 mmag) in the field of view. The number of suitable comparison stars depended on the number of the stars in the field of view with brightnesses greater than or similar to that of the target star, and varied from 2 to 9, with typical numbers being 4–5.

Table 2 is a log of the observations. The observing runs covered ~ 145 hrs, during which more than 8400 measurements were made.

3. Binary Modeling

The aims here are to make multicolor photometry of reasonable quality available, to provide preliminary models, and to supply enough information so interesting objects can be selected for follow-up work. Definitive values of the mass ratios will require radial velocity measurements (e.g., Terrell & Wilson 2005).

The light curves of the eight sdO/B or WD candidates show prominent reflection effects, characteristic of very close binaries with large temperature differences between components and equal or larger radii of companions compared to the hot primary stars. This is often observed in systems with hot compact primary stars, and late dwarf (dM) or even brown dwarf (BD) secondaries; some central stars of planetary nebula also show similar light curves (e.g., Jones & Boffin 2017). To constrain the nature of the primary star, the absolute Gaia magnitude M_G (Gaia Collaboration 2021) was used: this could be compared with the distribution of the known sdO/B+dM/BD system values. Three of the stars (ATL 0718+0739, ATL 0537-0049, and ATL 1748+0606) have absolute magnitudes typical of sdO/B+dM/BD systems ($M_G = 3.5$ – 5.5 mag; see Schaffenroth et al. 2019). However, ATL 2003+0838 has an absolute magnitude between those of sdB and WD stars (6.5 mag) and is probably a hot WD. A least-squares method was used to fit theoretical spectral energy distributions (SEDs) to literature values of photometry of the stars. Details of the calculation of the synthetic spectra and the fitting methodology can be found in Schaffenroth et al. (2021, 2022). Of course, the intrinsic variability of the stars adds to the uncertainties on the published photometry. This point was explored by Schaffenroth et al. (2022), who compared their SED fitting results to spectroscopically determined parameters, and found good agreement.

In this way we could constrain the temperature of the primary stars as well as the angular diameter and any color excess. Combining these results with the Gaia parallaxes, we additionally could derive the radii of the primary stars. Plots of the SED fits can be found in the figure set in Appendix B.

Light-curve modeling was performed with LCURVE, a code developed specifically for detached and accreting binaries containing a WD (for details see Copperwheat et al. 2010). This software has been used to analyze several detached WD +dM binaries (e.g., Parsons et al. 2010). The LCURVE code has

Table 2
Photometric Observing Log

Starting Time (HJD 2450000+)	Filters	Run Length (h)	<i>N</i>
ATL 0518			
9210.3036	<i>BVR</i>	3.6	120–122
9211.2864	<i>B</i>	4.3	402
9212.2921	<i>VR</i>	5.1	354–395
9602.3107	<i>V</i>	2.3	216
9603.2884	<i>R</i>	2.6	198
9605.2883	<i>B</i>	2.9	210
9606.2774	<i>I</i>	2.3	190
ATL 0537–0049			
8893.3570	<i>R</i>	2.2	532
8894.2842	<i>BR</i>	2.9	257–274
ATL 0718+0739			
8893.4604	<i>R</i>	1.8	448
8894.4135	<i>B</i>	2.1	518
ATL 0836–0802			
9301.2481	<i>VR</i>	3.7	75–95
9303.2325	<i>V</i>	2.9	137
9303.3660	<i>I</i>	1.9	84
9304.2295	<i>B</i>	1.6	38
9602.4260	<i>R</i>	2.3	187
9602.5219	<i>I</i>	2.2	180
9605.4342	<i>B</i>	1.3	73
9606.3862	<i>B</i>	2.1	140
ATL 0843–1159			
9200.5578	<i>VRI</i>	1.4	31
9201.5104	<i>VRI</i>	2.4	17–60
9210.4613	<i>VR</i>	3.3	97–108
9212.5186	<i>B</i>	2.2	45
ATL 1544–1816			
9292.5015	<i>VR</i>	3.6	34–40
9296.4925	<i>VR</i>	4.3	38–63
9438.2754	<i>I</i>	1.0	34
9440.2087	<i>I</i>	2.4	40
ATL 1748+0909			
9007.4114	<i>BVR</i>	3.4	32–43
9097.2185	<i>VR</i>	3.4	64–64
9099.2136	<i>BR</i>	3.1	45–55
9100.2127	<i>BVR</i>	4.1	47–50
ATL 1843+0226			
9008.4276	<i>RI</i>	5.4	80–81
9009.5167	<i>RI</i>	3.1	41–42
9010.5079	<i>VI</i>	3.4	39–42
9013.4339	<i>V</i>	4.6	76
9014.4327	<i>R</i>	3.1	74
ATL 1853+0339			
9014.5816	<i>RI</i>	2.1	57
9015.4324	<i>VRI</i>	3.5	39–41
9017.4102	<i>VRI</i>	5.4	61–64
9101.2289	<i>VRI</i>	2.0	21–23
9102.2149	<i>VRI</i>	3.9	41–45
9449.2580	<i>RI</i>	4.3	86–87
ATL 2003+0838			
9004.5059	<i>UBVR</i>	4.2	58–65
9005.4920	<i>UBVR</i>	4.3	40–69
9016.4652	<i>UBVR</i>	5.1	52–55
ATL 2028+0610			
9006.5626	<i>BVR</i>	2.7	51
9103.2622	<i>VR</i>	3.3	60–62

Note. The numbers of measurements across filters are in the last column.

also been successful in modeling sdB+WD or double WD systems showing ellipsoidal deformation (e.g., Kupfer et al. 2017). Therefore, LCURVE is ideally suited for systems containing hot blue objects.

The code calculates monochromatic light curves by subdividing the surface of each star into small elements with a geometry fixed by its radius as measured along the line from the center of one star toward the center of the companion. The flux of all visible elements is summed to obtain the observed flux at a given phase. A number of different effects that are observed in compact and normal stars are taken into account, such as Roche distortions due to the tidal influence of a massive, close companion, as well as limb darkening and gravitational darkening (e.g., Kallrath & Milone 2009).

As the light-curve model is based on many parameters, not all of them independent, as many parameters as possible were kept fixed when iterating toward a solution. The temperature derived by the fit to the SED or typical values for an sdB star were used. As the luminosity ratio of the components is very large, the temperature of the companion cannot be derived. We fixed the temperature of the companion to 3000 K, which is typical for a dM. Varying the temperature of the companion has no influence on the light-curve solutions. It was not possible to constrain the mass ratios of the systems, as the light curve is not sensitive to changes in the mass ratio; hence we assumed a canonical sdB mass ($0.47 M_{\odot}$; Heber 2016) and a mass corresponding to the radius of the companion (taken from Pecaut & Mamajek 2013). For the WDs, we assume $M = 0.5 M_{\odot}$ (Schaffenroth et al. 2018); the results are very similar for values in the range $0.4\text{--}0.6 M_{\odot}$. The quadratic limb darkening coefficients were taken from Claret & Bloemen (2011).

We used a simplex algorithm (e.g., Press et al. 1992), varying the starting guesses for parameters over a large range of values to find the best-fitting light-curve model, and varying the inclination and the relative radii of the components. The light curves in the different bands were either fitted separately or the fit from the highest S/N light curve was used and the other bands were used as a consistency check. More details on the light-curve fitting methodology can be found in Schaffenroth et al. (2021).

The results are summarized in Table 3 and are discussed in the next two sections of the paper. The model fits to the observations are illustrated in Figures 1–8; these are evidently excellent. The standard deviation of the scatter varies from 0.6% to 2.7%, with the mean being 1.5%.

4. The Eclipsing Binaries

4.1. ATL 0518-2308

Also known as HE 0516-2311 and EC 05160-2311, the star has been classified as a B-type hot subdwarf (sdB) based on spectroscopy (Edelmann 2003; O’Donoghue et al. 2013). Edelmann (2003) determined $T_{\text{eff}} = 31,000 \pm 300$ K and $\log g = 5.5 \pm 0.1$ by spectral model fitting. It was found as an eclipsing sdO/B candidate with a dM/BD companion (HW Vir system) by Schaffenroth et al. (2019). The star has been observed by the Transiting Exoplanet Survey Satellite (TESS; Ricker et al. 2015); the light curve can be seen in Baran et al. (2021).

Table 3
Summary of the Models Fitted to the Binary Stars

Name	q	r_1	r_2	T_1 (K)	T_2 (K)	i (deg)
Eclipsing systems						
ATL 0518–2308	0.34	0.235	0.227	31000	3000	71.9
ATL 0537–0049	0.42	0.311	0.255	28300	3000	66.8
ATL 0718+0739	0.34	0.282	0.257	40000	3000	82.7
ATL 0836–0802	0.34	0.275	0.210	26200	3000	69.3
Reflection-effect binaries						
ATL 1544–1816	0.16	0.022	0.199	38000	3000	35
ATL 1748+0909	0.32	0.215	0.283	34000	3000	62
ATL 2003+0838	0.15	0.068	0.313	50000	3000	36
ATL 2028+0610	0.26	0.297	0.278	27300	3000	44

Note. Subscripts 1 and 2, respectively, refer to the primary (hot, compact) and secondary (cool companion) stars. The temperatures of the primary stars were determined by SED fitting, with absolute radii following from absolute magnitudes. The temperatures of the secondary stars cannot be determined from the photometry and were fixed at 3000 K. The radii are given as fractions of the separation between the stars. The masses of primary stars were set at $\sim 0.5M_\odot$, while the masses of the secondary stars were deduced from tabled mass–radius data (Pecaut et al. 2012, Pecaut & Mamajek 2013).

Using the atmospheric parameters we could derive the radius and the mass of the sdB star by combining the fit of the SED with the Gaia parallax (see Schaffenroth et al. 2021 for more details on the method). We obtain a mass of $0.47_{-0.12}^{+0.17} M_\odot$, which is typical for a sdB, and a radius of $0.208_{-0.018}^{+0.021} R_\odot$. With the relative radii determined by the light-curve analysis (see Table 3), we can derive a separation of $0.89 \pm 0.08 R_\odot$ and a radius of the companion of $0.20 \pm 0.02 R_\odot$. This radius would imply a secondary star of spectral type about M5 and a mass of about $0.16 M_\odot$ —see e.g., Pecaut et al. (2012) and Pecaut & Mamajek (2013).⁶

The phased observational and theoretical light curves are plotted in Figure 1.

4.2. ATL 0537-0049

The star is in the candidate hot subdwarf catalog of Geier et al. (2019). It was also found to be a probable HW Vir system by Schaffenroth et al. (2019). The fit of the SED together with the Gaia parallax resulted in a temperature of $28,300_{-1600}^{+2100}$ K and a radius of $0.200 \pm 0.012 R_\odot$ giving a gravity $\log g$ of 5.51 ± 0.06 , when assuming a canonical sdB mass of $0.47 M_\odot$. Such atmospheric parameters are typical for a sdB. Combining this with the relative radii from the light-curve analysis, we can derive a system separation of $0.83 \pm 0.05 R_\odot$ and a companion radius of $0.26 \pm 0.02 R_\odot$, which would imply a spectral type of M4 and a mass of about $0.2 M_\odot$ (Pecaut et al. 2012; Pecaut & Mamajek 2013).⁷ The observed and model light curves are plotted in Figure 2.

4.3. ATL 0718+0739

ATL 0718+0739 is also a candidate hot subdwarf (Geier et al. 2019) and was considered a HW Vir system candidate by Schaffenroth et al. (2019). With an absolute magnitude

⁶ http://www.pas.rochester.edu/~emamajek/EEM_dwarf_UBVIJHK_colors_Teff.txt

⁷ http://www.pas.rochester.edu/~emamajek/EEM_dwarf_UBVIJHK_colors_Teff.txt

$M_G = 3.48 \pm 0.31$ mag the primary is at the bright end of the distribution of sdB luminosities suggesting it might have a higher temperature than the 26,000–31,000 K typical for sdBs (Schaffenroth et al. 2022). Unfortunately not enough good-quality photometric data are available for a definitive SED fit, so we will need spectroscopic data for a better characterization of the system. The light curve and a fit of the light curve assuming a temperature of 40,000 K are shown in Figure 3; the model results in Table 3 should only be considered plausible.

4.4. ATL 0836-0802

This star appears in the Geier et al. (2019) catalog of hot subdwarf candidates and the Schaffenroth et al. (2019) catalog of candidate HW Vir stars. The SED and the absolute magnitude obtained from the Gaia parallax confirm that the star is an HW Vir system with an sdB primary. Proceeding as for ATL 0537-0049, the properties of the sdB are $T = 26,200_{-2200}^{+2500}$ K, $R = 0.242_{-0.026}^{+0.031} R_\odot$, $\log g = 5.35 \pm 0.07$ with the assumption of a canonical $0.47M_\odot$ sdB mass. Using relative radii from the model fitting (Table 3) gives a binary separation of $0.89R_\odot$ and a radius of the secondary star of $0.184 \pm 0.024R_\odot$. The implied mass and spectral type of the secondary star are $M_2 = 0.162M_\odot$ and M5 (Pecaut et al. 2012; Pecaut & Mamajek 2013).⁸

The phase-folded observations together with model fits are plotted in Figure 4.

5. Reflection-effect Binaries

The four stars discussed in this section all show increases in the amplitude with increasing wavelength (Figures 5–8): in the least obvious case (ATL 2028+0610; Figure 8), the amplitudes are $6.9\% \pm 0.3\%$, $7.9\% \pm 0.2\%$, and $8.8\% \pm 0.2\%$ in B , V , and R , respectively. This demonstrates that the principal source of the variability is the changing aspect of reflection off a cool secondary star, rather than ellipsoidal deformation (e.g., Hilditch et al. 1996). For the noneclipsing reflection-effect systems, it is not possible to constrain the inclination, as there is a degeneracy with the radius of the companion (e.g., Hilditch et al. 1996). However, it is possible to distinguish between higher and lower inclinations using the shape of the reflection effect (e.g., Østensen et al. 2013; Schaffenroth et al. 2014), and the change in amplitude from filter to filter contains information about the temperature of the primary. Hence we searched for consistent solutions that fit the light curves in all different bands, assuming an inclination. This will not be a unique solution but can be used to estimate the nature of the companion under this assumption.

5.1. ATL 1544–1816

Gentile Fusillo et al. (2019) found an 0.76 probability that this star is a WD. This is also in accordance with the low luminosity ($M_G = 7.51 \pm 0.24$). The amplitude of the reflection effect varies from 20% in V to 35% in I . The large amplitude and the increase in amplitude with the wavelength of about 75% shows that the primary has to be a very compact hot star. The SED is not sensitive to the temperature in the likely temperature range, but it can be constrained by the wavelength dependence of the amplitude. The change in the amplitude

⁸ http://www.pas.rochester.edu/~emamajek/EEM_dwarf_UBVIJHK_colors_Teff.txt

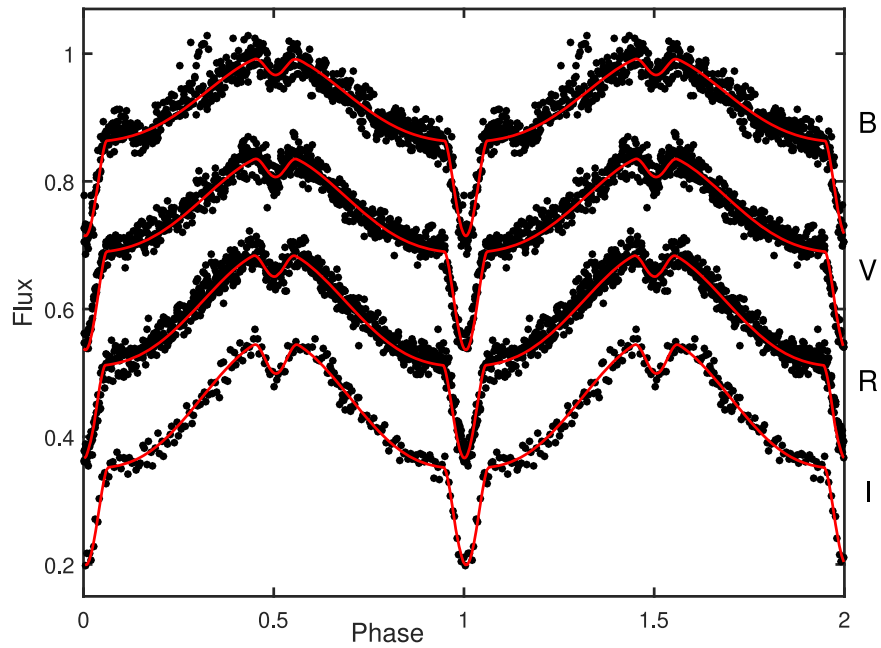


Figure 1. Phase-folded *BVRI* SAAO photometry of ATL 0518–2308 (dots) with model fits (lines). The fluxes have been normalized but have arbitrary zero-points.

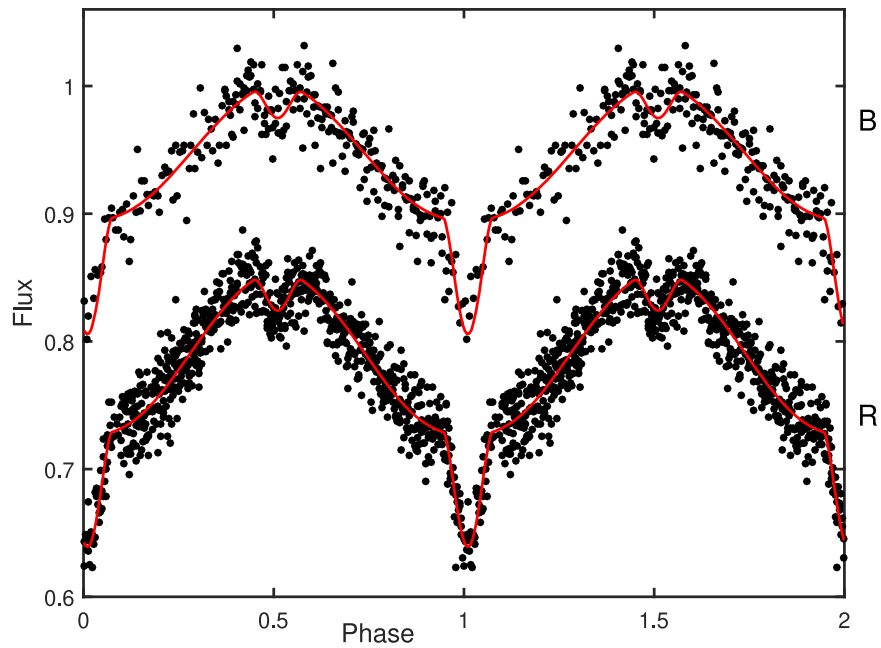


Figure 2. Phase-folded *BR* SAAO photometry of ATL 0537–0049 (dots) with model fits (lines). The fluxes have been normalized but have arbitrary zero-points.

from filter to filter is mostly dependent on the ratio of the flux of the primary star and the hot side of the companion. For a primary temperature of 38,000 K, we found a solution fitting the light curves in all three filters well. There is a degeneracy between the inclination and radius of the primary and secondary. However, the nearly sinusoidal shape of the reflection effect suggests that the inclination cannot be too high. So we assumed an inclination of $\sim 35^\circ$. (Taking $i = 60^\circ$ gives notably worse model fits). With the derived temperature and the assumed inclination given in Table 3 as well as the distance to the system from the Gaia parallax the radius of the primary can be constrained to about $0.04R_\odot$, which is typical for a WD. Using the relative radii determined by the light-curve

analysis, we obtain a radius of $0.11R_\odot$ for the companion, which suggests an M8 spectral type, close to the hydrogen burning limit. The determination of the radius of the primary star however depends on the temperature used, and so this has to be confirmed with spectroscopy. A higher assumed inclination will result in a smaller radius of the companion and vice versa. A higher S/N light curve will be necessary to better constrain the inclination.

Figure 5 shows the observed and model light curves.

5.2. ATL 1748+0909

Although ATL 1748+0909 appears in the WD candidate catalog of Gentile Fusillo et al. (2019), the authors assign a

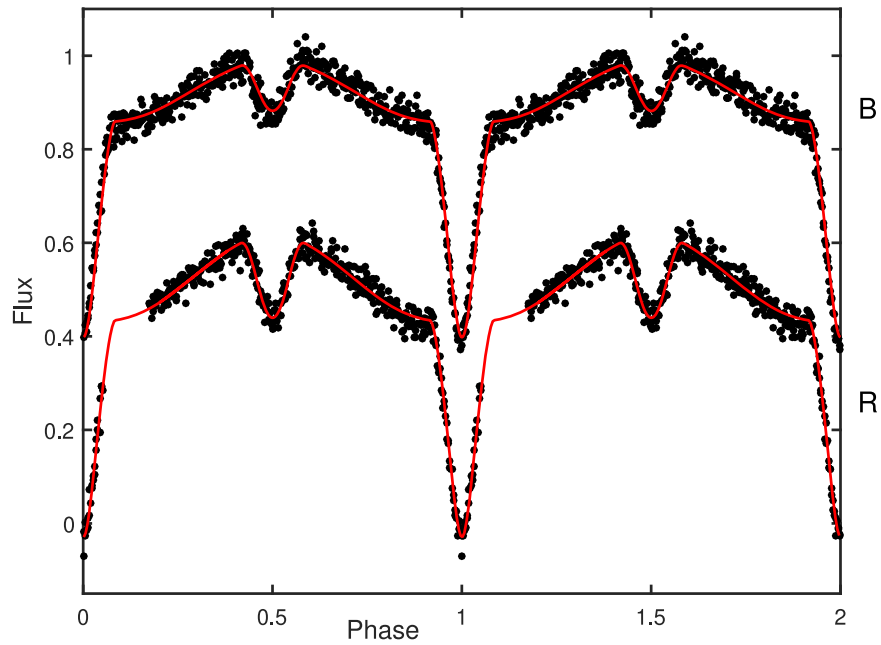


Figure 3. Phase-folded *BR* SAAO photometry of ATL 0718+0739 (dots) with model fits (lines). The fluxes have been normalized but have arbitrary zero-points.

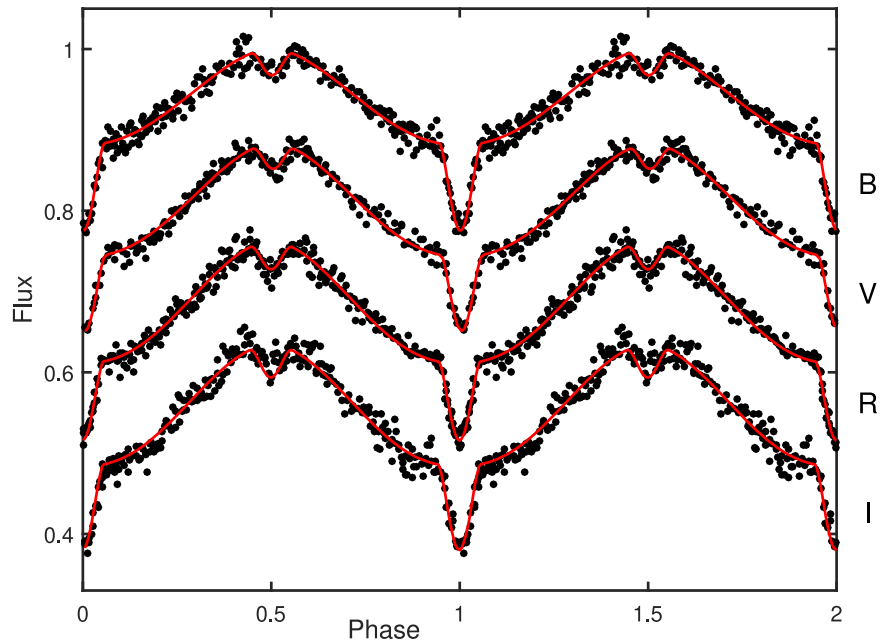


Figure 4. Phase-folded *BVRI* SAAO photometry of ATL 0836-0802 (dots) with model fits (lines). The fluxes have been normalized but have arbitrary zero-points.

negligible (0.005) probability that this star with $M_G = 5.10 \pm 0.26$ mag is indeed a WD. The model results in Table 3 suggest that its classification as a sdB by Geier et al. (2019) is correct. The *R*-filter amplitude is 0.28 mag, which is quite large for a sdO/B+dM system. This suggests that the sdB is hotter and/or smaller than a typical sdB. This is confirmed by the SED fit, which results in a temperature of $34,000^{+7000}_{-4000}$ K and a radius of $0.134^{+0.022}_{-0.019} R_\odot$. Assuming a mass of $0.47 M_\odot$ we get a surface gravity of $\log g = 5.86 \pm 0.12$. The flat bottom of the reflection effect suggests a higher inclination; we assumed $i = 62^\circ$ ($i = 40^\circ$ gave a poorer fit). We can then derive the separation of the system as $a = 0.62 \pm 0.10 R_\odot$ and a companion radius of

$0.176 \pm 0.032 R_\odot$. This implies an M5 companion with a mass of about $0.15 M_\odot$.

The phased data and the model fits are plotted in Figure 6.

5.3. ATL 2003+0838

According to Gentile Fusillo et al. (2019) the probability that ATL 2003+0838 is a WD is 0.28. Although the star also has an entry in the Geier et al. (2019) hot subdwarf candidate catalog, the physical properties ($M_G = 6.54 \pm 0.035$ mag) and very large reflection-effect amplitude change of 25% in *U* and 55% in *R* suggest that the primary star is a very hot WD. For a temperature of about 50,000 K we could obtain a good model fit of the light curve in all filters. Using this temperature we get

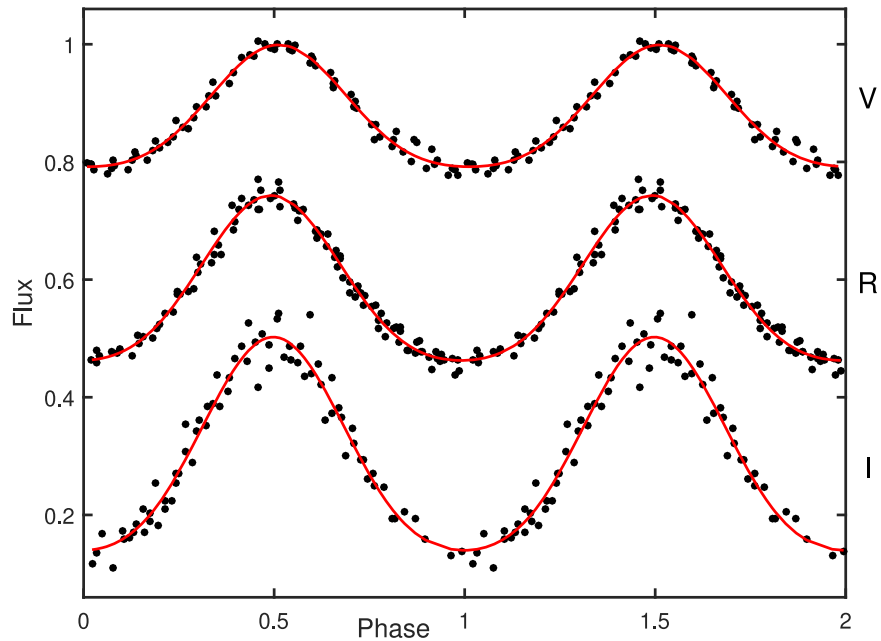


Figure 5. Phase-folded *VRI* SAAO photometry of ATL 1544–1816 (dots) with model fits (lines). The fluxes have been normalized but have arbitrary zero-points.

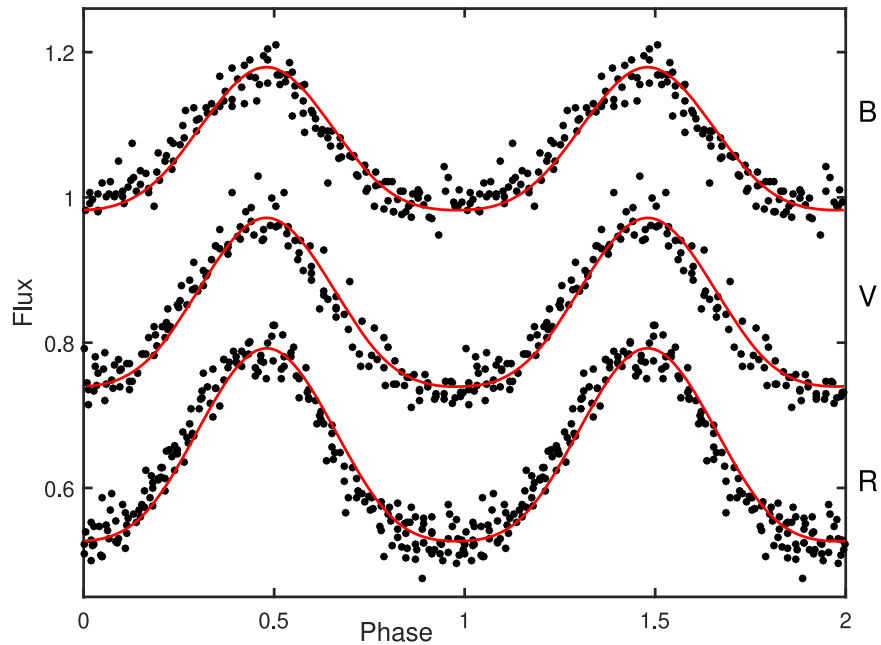


Figure 6. Phase-folded *BVR* SAAO photometry of ATL 1748+0909 (dots) with model fits (lines). The fluxes have been normalized but have arbitrary zero-points.

a radius of $0.059 \pm 0.003 R_{\odot}$ for the WD and a companion radius of $0.27 R_{\odot}$. However, this depends on the assumed WD temperature; hence spectroscopy is necessary to better constrain the companion properties. Moreover, as no eclipses are visible, the inclination is also difficult to determine by the light-curve fit. This is especially true at lower inclinations, as the light-curve shape due to the reflection effect is sinusoidal and a different inclination will also result in a different radius for the companion. We note that no physical models could be fitted assuming $i = 20^{\circ}$, while $i = 60^{\circ}$ led to poor light-curve fits.

Observed and theoretical light curves can be seen in Figure 7.

5.4. ATL 2028+0610

This star is a hot subdwarf candidate (Geier et al. 2019). With the model parameters in Table 3, $M_G = 4.57 \pm 0.082$ mag, and a modest *R*-filter amplitude of 0.10 mag, it seems to be a typical sdB+dM system. This is confirmed by the SED fit assuming a canonical-mass sdB ($T_{\text{eff}} = 27,300^{+1900}_{-1600}$ K, $R_{\text{sdB}} = 0.195 \pm 0.012 R_{\odot}$, $\log g = 5.53 \pm 0.05$). Using the relative radii derived from the light-curve fit and assuming an inclination of 44° this would suggest an M5 companion with a radius of $0.18 \pm 0.1 R_{\odot}$ and a mass of $0.15 \pm 0.1 M_{\odot}$. Taking $i = 60^{\circ}$ leads to a model of similar quality, while an inclination as low as 20° can be ruled out, as the required secondary star radius would be unphysically large. Time-resolved

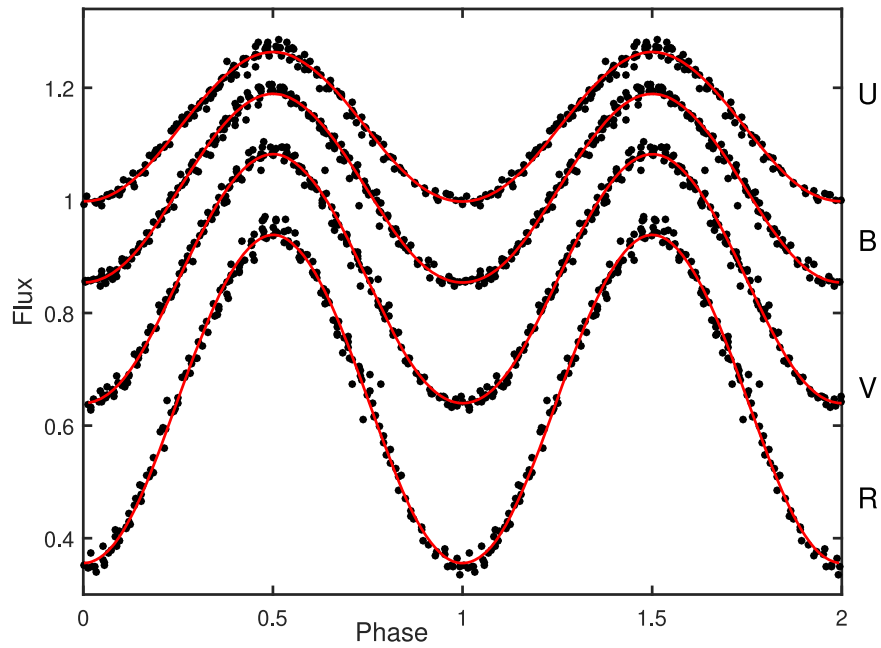


Figure 7. Phase-folded *UBVR* SAAO photometry of ATL 2003+0838 (dots) with model fits (lines). The fluxes have been normalized but have arbitrary zero-points.

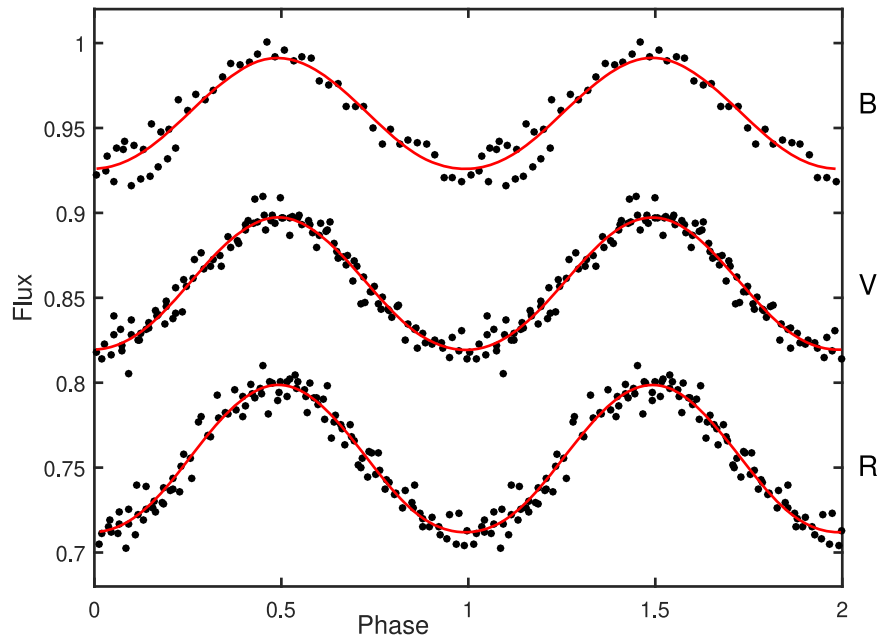


Figure 8. Phase-folded *BVR* SAAO photometry of ATL 2028+0610 (dots) with model fits (lines). The fluxes have been normalized but have arbitrary zero-points.

spectroscopy to determine the radial velocity curve and a higher S/N light curve are necessary to confirm the model. See Figure 8 for the observational and model light curves.

6. Three Pulsating Stars

ATL 1843+0226 and ATL 1853+0339 were originally selected from the ATLAS variable star catalog on the basis of their very red colors (see Table 1) as candidate late-type binary stars. ATL 0843–1159, on the other hand, is classified by Heinze et al. (2018) as a close binary system. Closer scrutiny of their light curves and other properties suggest that all three are likely δ Scuti pulsators (e.g., Guzik 2021, and numerous references therein).

Table 4 contains the physical properties and reddening of the three stars derived from photometry covering the visible and near-infrared parts of the spectrum, extracted from the Vizier database.⁹ Original sources of measurements include the AAVSO Photometric All-Sky Survey (APASS; Henden et al. 2015), Gaia (Gaia Collaboration 2021), the Panoramic Survey Telescope and Rapid Response System (Pan-STARRS; Chambers et al. 2016), the SkyMapper Southern Survey (Wolf et al. 2018; Onken et al. 2019), the Two Micron All-Sky Survey (2MASS; Skrutskie et al. 2006), the Wide-field Infrared Survey Explorer (WISE; Wright et al. 2010), and the Galaxy Evolution Explorer (GALEX; Bianchi et al. 2011). Use was

⁹ <https://vizier.u-strasbg.fr/viz-bin/VizieR>

Table 4
Physical Properties, Derived from Absolute Photometry, of the Three Stars Discussed in Section 6

Star	A_V (mag)	T_{eff} (K)	$\log g$ (dex)	M_{bol} (mag)	$\sigma_{M(p)}$ (mag)	SpT	SpM	n
ATL 0843–1159	0.10	7640(150)	4.0(0.6)	2.5(0.1)	0.09	A7	F0	23
	0.30(0.11)	7940(245)	3.7(1.0)	2.3(0.2)		A6	A9	
	0.10	7550(99)	4.5(0.5)	2.5(0.1)		A8	F0	
	0.32(0.06)	7830(116)	4.3(0.3)	2.34(0.1)		A7	A9	
ATL 1843+0226	5.36	7680(194)	5.1(1.2)	1.6(0.3)	0.26	A7	A3	12
	5.42(0.27)	7810(649)	5.1(1.1)	1.6(0.4)		A7	A3	
ATL 1853+0339	6.36	7250(186)	5.9(0.6)	−1.4(0.3)	0.27	F0	B7	13
	7.20(0.29)	9540(1550)	5.8(0.5)	−2.3(0.6)		A0	B5	

Note. For each star, the first line in the Table assumes extinction fixed at the value extracted from Green et al. (2018), while the second line reports results with A_V as a free parameter. The contribution of the parallax uncertainty to the error on the bolometric magnitude is denoted by $\sigma_{M(p)}$. SpT and SpM are spectral types deduced, respectively, from the temperature and bolometric magnitude estimates. The last column gives the number of photometric measurements taken into account. Bolometric corrections for ATL 0843–1159 and ATL 1853+0339 assumed solar metallicity, while $[\text{Fe}/\text{H}] = -0.75$ for ATL 1843+0226, in accordance with its spectroscopic metallicity determination (see Table 5).

also made of parallaxes from Gaia Collaboration (2021), the extinction law $f_\lambda = A_\lambda/A_V$ from Schafly et al. (2016), the cumulative reddening map of Green et al. (2018)¹⁰, and bolometric corrections from the Modules for Experiments in Stellar Astrophysics (MESA) Isochrones and Stellar Tracks website.¹¹ Online availability of these sources is gratefully acknowledged.

Photometry was used to estimate the luminosity, temperature, and reddening of each star. This is conveniently done by minimizing the differences between the bolometric magnitudes estimated from the individual photometric measurements, with the objective function being the sum of squared residuals

$$\begin{aligned}
 \text{SS} &= \sum_{\lambda}^{N_{\lambda}} [M_{\text{bol}} - \widehat{M}_{\text{bol},\lambda}]^2 \\
 &= \sum_{\lambda}^{N_{\lambda}} \{M_{\text{bol}} - [(m_{\lambda} + 5 + 5 \log_{10} p) - A_V f_{\lambda} + BC_{\lambda}]\}^2
 \end{aligned}
 \tag{1}$$

where λ is wavelength; m_{λ} are the photometric measurements; A_V and f_{λ} , respectively, are the V -filter absorption and the extinction law; M_{bol} and BC_{λ} the bolometric magnitude and bolometric correction, respectively; and p is the parallax. The notation $\widehat{M}_{\text{bol},\lambda}$ indicates the bolometric magnitude estimated from the measurement through the filter with an effective wavelength λ .

The uncertainties were estimated using a bootstrapping procedure—see Koen (2022) for details. The spectral types corresponding to, respectively, the temperature and bolometric magnitude were taken from Pecaut et al. (2012) and Pecaut & Mamajek (2013);¹² these are designated “SpT” and “SpM” in Table 4.

A discussion of the results for the individual stars follows.

6.1. ATL 0843–1159

Two of the photometric measurements (APASS g' and r') give outlying (by ~ 0.2 mag) estimates of M_{bol} . If these are excluded, the second set of solutions in Table 4 is obtained.

¹⁰ <http://argonaut.skymaps.info/>

¹¹ http://waps.cfa.harvard.edu/MIST/model_grids.html#bolometric

¹² http://www.pas.rochester.edu/~emamajek/EEM_dwarf_UBVIJHK_colors_Teff.txt

The derived temperatures and luminosities suggest that the star is of late A/early F spectral type. The line-of-sight absorption is 0.1–0.3 mag.

The light curves of ATL 0843–1159 (Figure 9) resemble those of RR Lyrae stars. However, the short period (~ 1.4 hr) and value of the absolute magnitude are consistent with the star being a high-amplitude δ Scuti (HADS) pulsator. The APASS observation $V = 14.2$ can be corrected for absorption to $A_V \approx 14.0$ mag, and $M_V = 2.3$ mag follows from the Gaia parallax. Furthermore, using the recent period–luminosity relation for δ Scuti stars

$$M_V = -2.94 \log_{10} P - 1.34$$

(Ziaali et al. 2019), the predicted absolute magnitude of the star is $M_V = 2.3$ mag. Examination of Figure 5 in Ziaali et al. (2019) suggests that evolutionarily it is close to the main sequence.

6.2. ATL 1843+0226

The apparent brightness of the star increases monotonically with increasing wavelength, from Pan-STARRS g to WISE $W3$, except for the $W2$ measurement, which is anomalously faint. This measurement also leads to a bolometric magnitude estimate ~ 0.5 mag fainter than that associated with the rest of the photometry. It was therefore excluded in calculating the results in Table 4. ATL 1843+0226 is of similar spectral type to ATL 0843–1159, but the reddening is substantial.

Two successive exposures of 15 minutes each on the star were also obtained with the Robert S. Stobie (RSS) spectrograph of the 10 m Southern African Large Telescope, covering 3400–6400 Å. The spectra were co-added, and standard reduction techniques were applied, including calibration using a spectrophotometric standard. The total reduced spectrum of ATL 1843+0226 was analyzed with use of the Fitting Binary Stars (FBS; Kniazev et al. 2020) package. This software was developed to determine the parameters of individual components of binary systems such as the effective temperature T_{eff} , surface gravity $\log g$, projected rotational velocity $v \sin i$, metallicity $[\text{Fe}/\text{H}]$, and heliocentric radial velocity V_{hel} , as well as the color excess $E(B - V)$ of the system. The software simultaneously approximates the observed spectrum by a model, which is obtained by interpolating over the grid of theoretically calculated high-

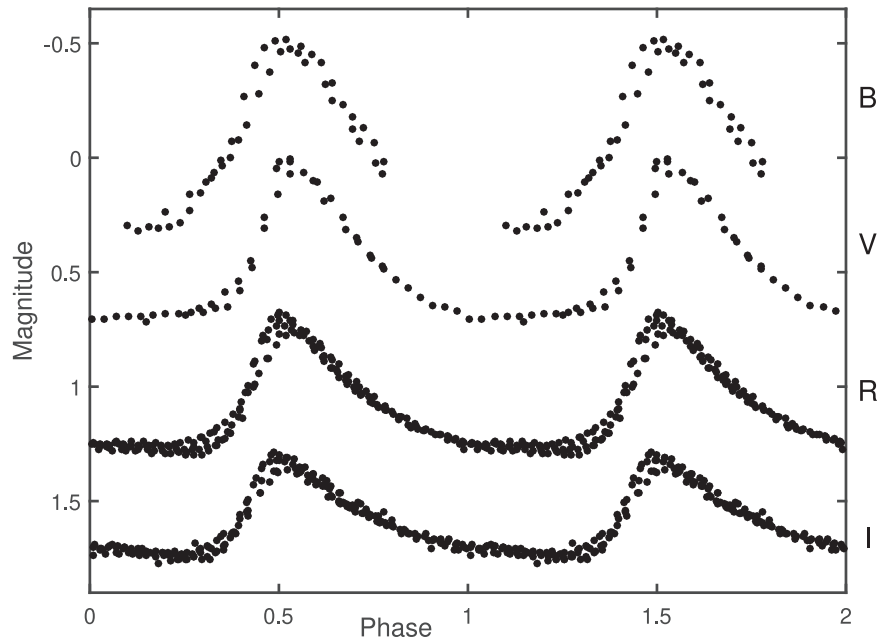


Figure 9. Phase-folded *BVRI* SAAO photometry of ATL 0843–1159. The zero-points of the light curves are arbitrary.

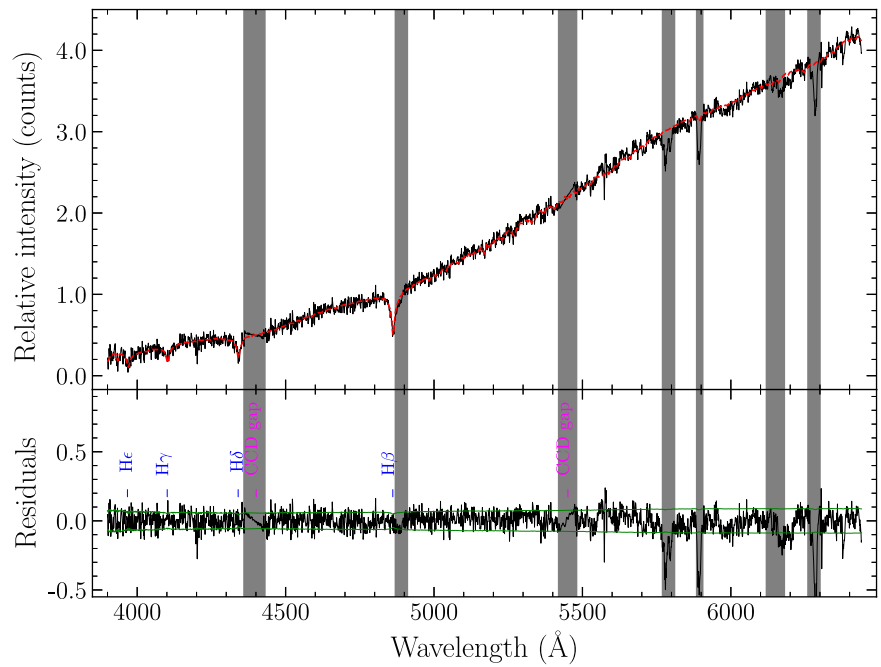


Figure 10. Results of modeling of the fully reduced spectrum of ATL 1843+0226. Upper panel: comparison of the observed spectrum (solid black line) with the best-fitting model (red dashed line) obtained with the FBS software. The gray vertical areas show spectral regions excluded from the spectral fit because of their contamination by most prominent diffuse interstellar bands. Bottom panel: difference between the observed and model spectra (black noisy line). The green solid lines indicate 1σ errors in the observed spectrum. The positions of identified Balmer lines and CCD gaps are indicated.

Table 5
Results of Fitting Main-sequence Models to the Spectroscopic Observations of ATL 1843+0226

Spectral Type	T_{eff} (K)	$\log g$ (dex)	[Fe/H]	v_r (km s ⁻¹)	$E(B - V)$ (mag)	A_V (mag)
A9-F0V	7300 (500)	4.2 (0.25)	-0.70 (0.15)	43 (7)	1.75 (0.05)	5.4

Note. Uncertainties are given in brackets.

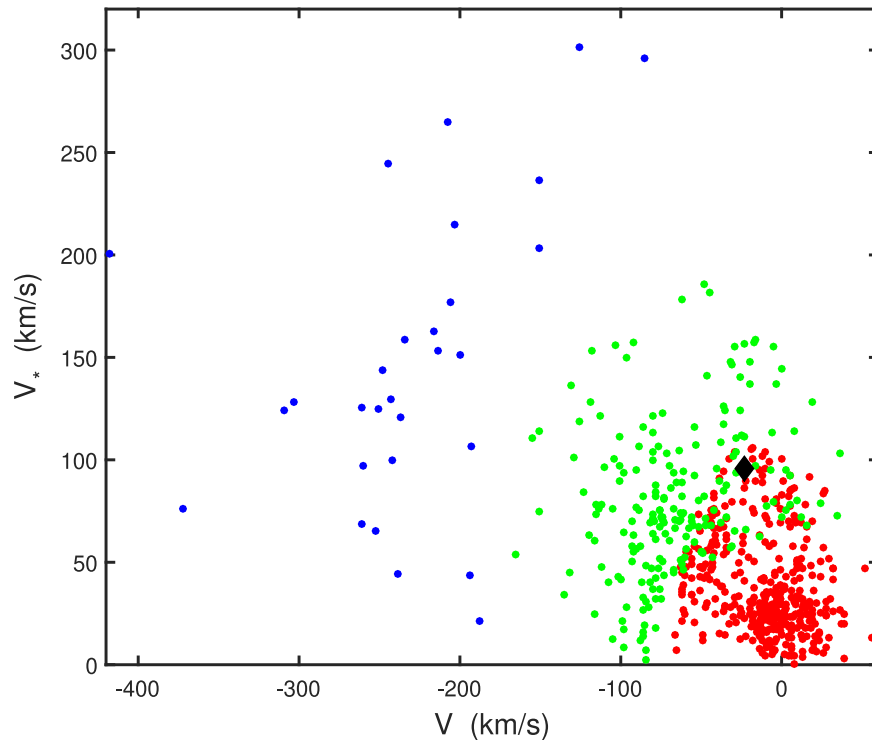


Figure 11. Toomre diagram, showing the positions of 706 field stars from Bensby et al. (2014). Red, green, and blue dots, respectively, indicate stars in the thin disk, thick disk, and halo. The velocity components of ATL 1843+0226 are shown by the black diamond.

resolution stellar spectra, and convolves it with a function that takes the broadening and wavelength shift into account. In case of a single star the fitting routine uses one model spectrum for the single star. In our case the set of PHOENIX models (Husser et al. 2013) was used, previously convolved to match the RSS instrumental resolution. As shown in Muhie et al. (2021), FBS modeling of RSS spectra performs well in the total range of metallicities from $-3 \leq [\text{Fe}/\text{H}] \leq 0$ with 1σ error ~ 0.20 dex.

The model spectrum fitting results are shown in Figure 10 and Table 5. Assuming

$$R_V = A_V / E(B - V) = 3.1$$

(e.g., Fitzpatrick 1999), $A_V = 5.43$, in very good agreement with the photometrically derived results and the value from the cumulative absorption map. The temperature-based spectral type of A7 is also close to the A9–F0 classification.

Given the information above, it is concluded that the star is either an HADS or an SX Phoenicis pulsator (e.g., McNamara 1995). The low metallicity is evidence in favor of the latter; we turn to kinematics to further discriminate between the two possibilities.

The Galactic coordinates of ATL 1843+0226 are $\ell = 34.2542$, $b = 2.7911$, i.e., the star is close to the Galactic plane. In fact, given the 1.73 ± 0.21 kpc distance from the Sun (from the parallax in Table 1), its distance above the plane is only 84 ± 10 pc, which would place it in the thin disk. The Gaia parallax and proper motions of the star can be used to calculate space velocities $U = 88.2$, $V = -23.3$, $W = -37.0$ km s^{-1} (using the formulation of Johnson & Soderblom 1987, with corrections for the solar motion taken from Coşkunoğlu et al. 2011). Also of interest is the total velocity $V_t = \sqrt{U^2 + V^2 + W^2} = 98.5$ km s^{-1} .

Toomre diagrams are plots of $V_* = \sqrt{U^2 + W^2}$ (95.7 km s^{-1} , in the case of ATL 1843+0226) versus V . Figure 11 is a recreation of Figure 9 in Kovalev et al. (2019), to which the (V, V_*) position of ATL 1843+0226 has been added. Shown are the positions of the thin disk, thick disk, and halo stars. Data were taken from Bensby et al. (2014), and the classification criteria of Kovalev et al. (2019; their Appendix C) were applied. Given the large value of V_t , together with the low metallicity, it may be concluded that ATL 1843+0226 is an SX Phe star near the thin disk/thick disk boundary.

Some insight into the nature of the pulsation can be gained from the pulsation constant Q given by

$$\log Q = -6.454 + \log P + 0.5 \log g + 0.1 M_{\text{bol}} + \log T_{\text{eff}}$$

where P is the pulsation period in days (e.g., Breger & Bregman 1975). Substituting with the parameter values from Table 5, $Q \approx 0.034$, which implies pulsation in the fundamental radial mode (Fitch 1981). This is consistent with the asymmetry in the light curve and the large amplitude (e.g., McNamara 1995).

There is a slight bump visible in the light curves in Figure 12, near light maximum on the descending branch. This phenomenon is well known in Cepheid and RR Lyrae pulsators (see, e.g., the summaries in Paxton et al. 2019). We could find only one instance of an SX Phe variable—XX Cyg—for which (transient) light-curve bumps have been reported (e.g., Sadun & Ressler 1986; Blake et al. 2003).

Most SX Phe stars have been found in globular clusters, in the form of blue stragglers; examples in the field being relatively rare (e.g., Jeon et al. 2010).

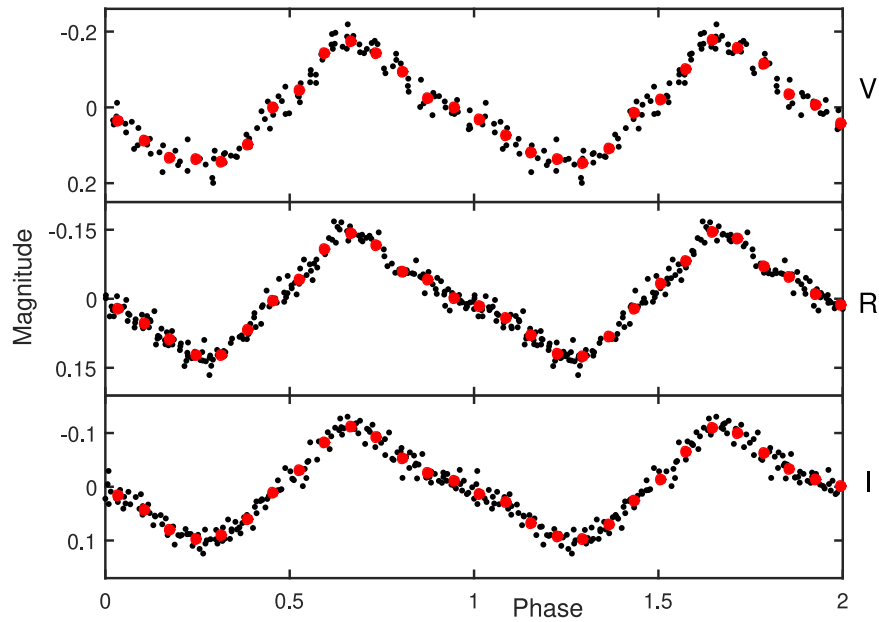


Figure 12. Phase-folded SAAO light curves of ATL 1843+0226. Small (black) dots are raw observations, and large (red) dots are the averages of phase bins with width 0.07. Note that the vertical scales on the panels are different the better to show the nonsinusoidal nature of each light curve—the panel heights are 0.51, 0.42, and 0.34 mag from top to bottom. The zero-points are arbitrary.

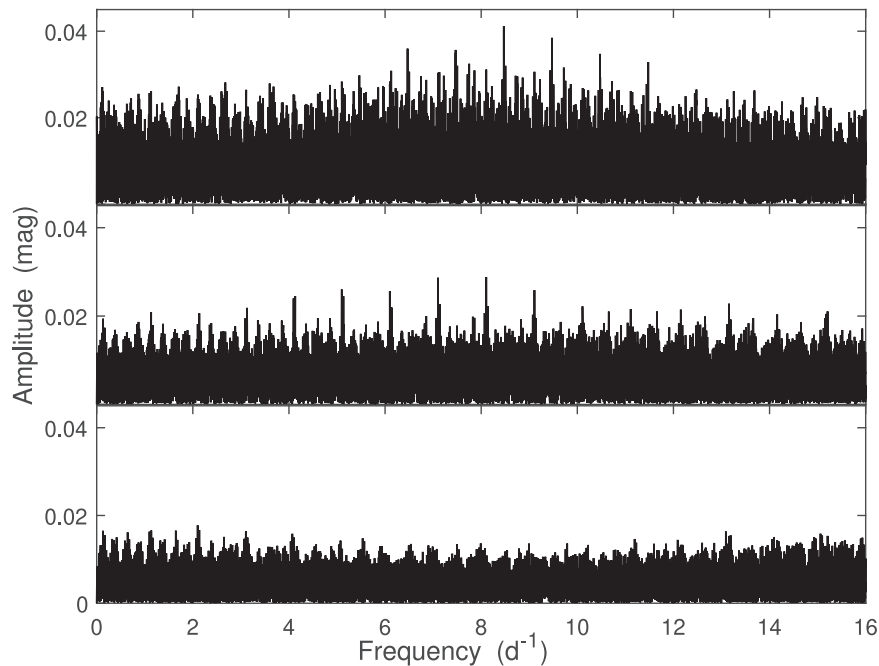


Figure 13. Top panel: amplitude spectrum of the *o* filter ATLAS photometry of ATL 1853+0339. Middle panel: amplitude spectrum of the residuals after whitening by the most prominent frequency (8.47068 day^{-1}) in the top panel. Bottom panel: amplitude spectrum after whitening the photometry by frequencies 8.47068 and 8.1052 day^{-1} .

6.3. ATL 1853+0339

This star is even more heavily reddened than ATL 1843+0226; dust absorption estimates in Table 4 differ by $\sim 10\%$ and are in the range 6.4–7.2 mag. The Galactic latitude is only $1^\circ 20'$, and at a distance of 2.76 ± 0.35 kpc (from the parallax in Table 1), the distance above the plane is a mere 58 ± 7 pc.

The estimated luminosity of the star is much larger than that of a main-sequence star of the estimated temperature. Invoking a companion of comparable brightness does not come close to resolving the problem. A possible explanation is that the star is

evolved. It is noted that ATL 1853+0339 is in a catalog of luminous OBA candidates selected on the basis of photometry, parallaxes, and kinematics (Zari et al. 2021).

The tallest peak in the periodogram of the somewhat noisy and sparse ($N = 70$) ATLAS *c* filter observations of the star is at 9.47 day^{-1} , which is an alias of the catalog value $f = 1/0.118055 = 8.4706 \text{ day}^{-1}$. Prewhitening by this frequency leads to an essentially featureless spectrum. Figure 13 (top panel) shows an amplitude spectrum of the ATLAS *o* filter photometry; the largest peak is indeed at 8.4708 day^{-1} . Interestingly, prewhitening by this frequency reveals the

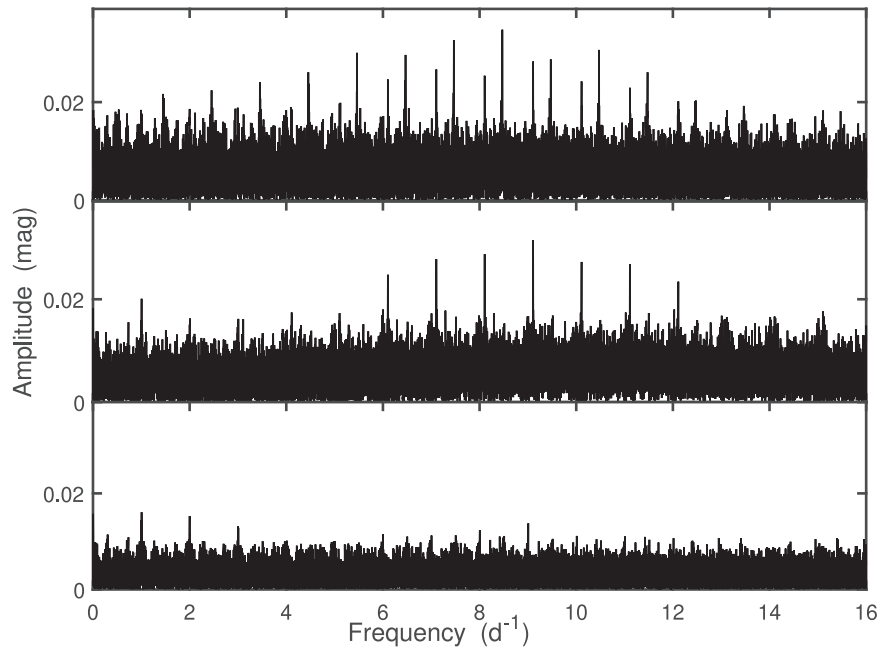


Figure 14. Top panel: amplitude spectrum of the r -filter ZTF photometry of ATL 1853+0339. Middle panel: amplitude spectrum of the residuals after prewhitening by the most prominent frequency (8.47069 day^{-1}) in the top panel. Bottom panel: amplitude spectrum after prewhitening the photometry by frequencies 8.47069 and 9.10779 day^{-1} .

presence of a second periodicity. The largest peak in the residual spectrum (middle panel of Figure 13) is at a frequency of 8.1052 day^{-1} , though this is by no means secure due to aliasing. Note that prewhitening by both frequencies leaves an essentially flat spectrum characteristic of white noise (bottom panel of Figure 13).

Additional insight can be gained by studying the Zwicky Transient Facility (ZTF; Bellm et al. 2019) observations of ATL 1853+0339. The star is included in the ZTF catalog of periodic variable stars (Chen et al. 2020) with $P = 0.2361$ days (i.e., a frequency of 4.236 day^{-1}). There are 629 ZTF r -filter measurements of the star. These cover a time baseline of 3.2 yr and are generally “dense,” in the sense that the time interval between successive observations is mostly less than a day (419 out of 628). An amplitude spectrum of the ZTF photometry is plotted in the top panel of Figure 14. It is evident from the complicated pattern of peaks in the interval $4 < f < 12 \text{ day}^{-1}$ that there is more than one periodicity in the data. The largest peak is at a frequency of 8.47069 day^{-1} , which is in excellent agreement with $f = 8.47063 \text{ day}^{-1}$ in the ATLAS variable star catalog. The spectrum of the residuals after prewhitening by the former frequency is in the middle panel of the figure; most of the peaks in the top panel have disappeared, confirming that they were at aliases of the 8.47069 day^{-1} periodicity. The largest peak in the middle panel is at 9.10788 day^{-1} , i.e., a 1 day^{-1} alias of the second frequency found in the ATLAS o data. If $f = 9.01788 \text{ day}^{-1}$ is also prewhitened from the g -filter data the spectrum in the bottom panel of Figure 14 results. The most prominent peaks in this final spectrum are at 1 day^{-1} and its aliases, suggesting slight zero-point differences for different nights.

It should be noted that the level of the residual (i.e., noise) spectrum in the bottom panel of Figure 14 is $\sim 30\%$ lower than that in the bottom panel of Figure 13. This is primarily due to the larger number of data in the ZTF photometry.

Analysis of the SAAO data—which are dense within individual nights—confirms that the aliases identified in the ZTF data are the correct ones. Using these two frequencies as starting values, the model

$$m(t) = a_0 + a_1 \cos(2\pi f_1 t + \phi_1) + a_2 \cos(2\pi f_2 t + \phi_2) + \text{error}$$

was fitted to the r photometry. The results were $f_1 = 8.47069(3) \text{ day}^{-1}$, $f_2 = 9.10779(4) \text{ day}^{-1}$, $a_1 = 0.041 \pm 0.002 \text{ mag}$, and $a_2 = 0.033 \pm 0.002 \text{ mag}$. The amplitude of the largest peak in the residual spectrum is 0.014 mag , and prewhitening by its frequency (1 day^{-1}) leaves a featureless spectrum with a mean level of 3.3 mmag .

Given that the star is much brighter in the red, it is no surprise that the ZTF g -filter photometry is less informative: aside from the largest peak (0.047 mag) at $f = 8.47067 \text{ day}^{-1}$, the spectrum is noise-dominated.

The two frequencies extracted from the ZTF photometry can now be fitted to the SAAO observations (see Figure 15 for an example); this gives more detailed information about the dependence of the amplitudes on the wavelength. Interestingly, spectra of the residuals (Figure 16) show two broad humps of excess power, centered roughly on 6 day^{-1} and 13 day^{-1} . The highest peaks are at 7.23 and 13.18 day^{-1} (I), 6.18 and 13.19 day^{-1} (R), 5.71 and 13.21 day^{-1} (V). Obviously aliasing prohibits more definitive results, but it seems clear that there are two additional periodicities in the data, one with a probable frequency $\sim 13.2 \text{ day}^{-1}$, and the other at a lower frequency in the approximate range $5.5\text{--}7.5 \text{ day}^{-1}$.

The amplitudes associated with all four periodicities are listed in Table 6. For three of the four frequencies, the amplitude does not vary much over the effective wavelength range $\sim 5500\text{--}7900 \text{ \AA}$ covered by the VRI filters. The exception is $f = 9.11 \text{ day}^{-1}$, for which the amplitude increases with decreasing wavelength. The reader’s attention is also drawn to the anomalously large g -filter amplitude of the 8.47 day^{-1} mode.

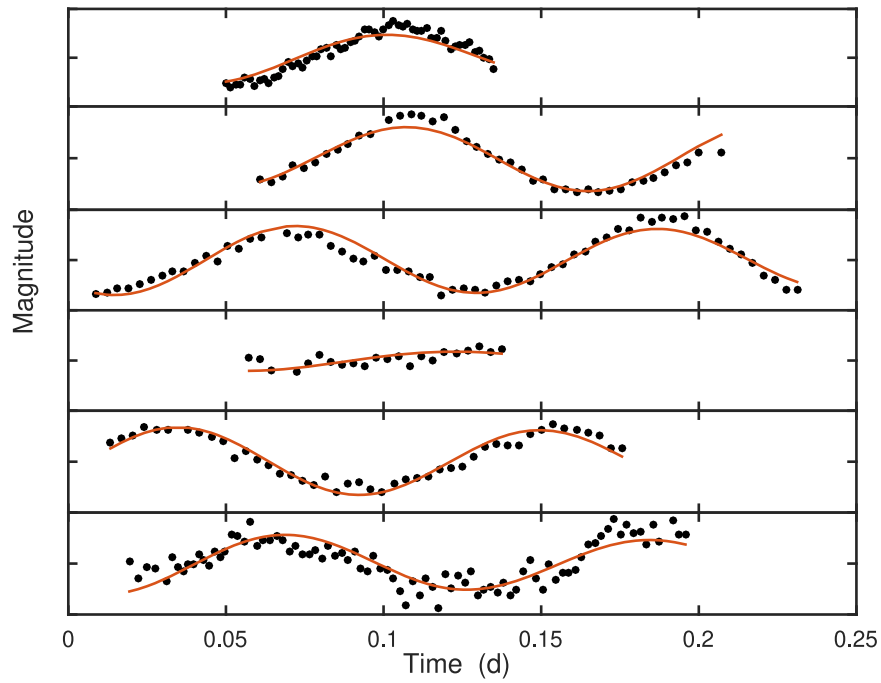


Figure 15. Two-frequency fit (red lines) to the six sets of SAO *R*-filter observations of ATL 1853+0339 (dots). The vertical width of each panel is 0.2 mag. Both the magnitude and time zero-points for each panel are arbitrary.

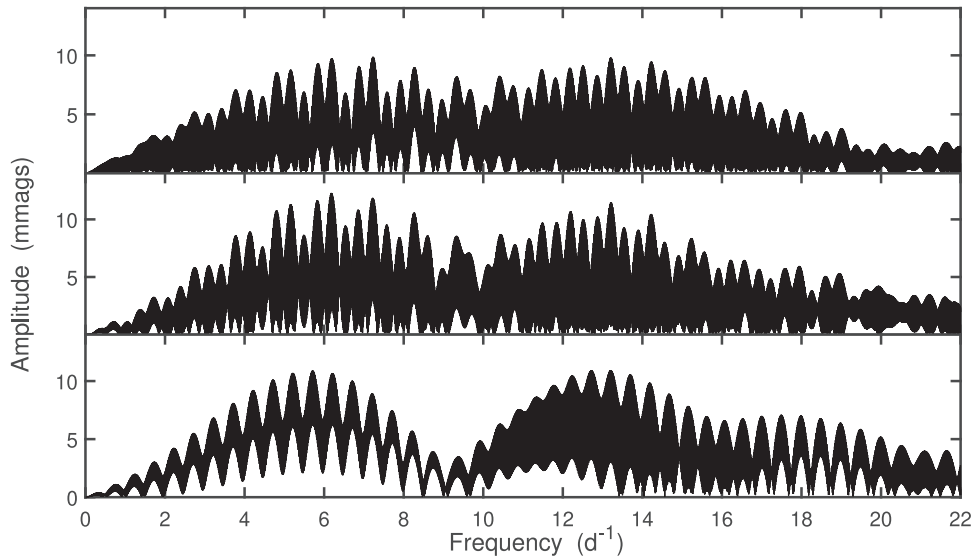


Figure 16. Amplitude spectra of the residuals left after prewhitening the SAO photometry of ATL 1853+0339 by frequencies 8.47069 and 9.10779 day⁻¹. From top to bottom: *I*-, *R*-, and *V*-filter observations.

Table 6
Amplitudes (in Millimagnitudes) of the Periodicities in the Photometry of ATL 1853+0339

Frequency (day ⁻¹)	Filter						
	<i>g</i>	<i>c</i>	<i>V</i>	<i>r</i>	<i>R</i>	<i>o</i>	<i>I</i>
8.47069	47	61	45(2)	41(2)	44(2)	40(4)	41(1)
9.10779	35(2)	33(2)	26(2)	24(4)	25(1)
13.2	11	...	9	...	9
5.7–7.2	10	...	12	...	10

Note. The uncertainty in the last digit is given in brackets, for those amplitudes determined by model fitting; other amplitudes are the spectral peak heights.

Given the relatively short period (2.8 hr) and high temperature, two candidate classes of pulsating stars come to mind: β Cephei and δ Scuti. The former can probably be ruled out by the fact that β Cephei stars are of early B spectral types (B0–B2.5; see, e.g., Stankov & Handler 2005), i.e., most likely considerably hotter than ATL1853+0339. δ Scuti stars, on the other hand, also appear unlikely as the luminosity of the star is $\log(L/L_{\odot}) = 2.4\text{--}2.8$, which, for example, exceeds that of all stars in the well-populated $\log L\text{--}T_{\text{eff}}$ diagram of Ziaali et al. (2019; see their Figure 5). However, Balona (2018) calculated the luminosities of δ Scuti stars in the Kepler field and found a scattering of these pulsators with $\log(L/L_{\odot}) > 2$.

The rate of increase in the amplitudes with decreasing wavelength (Table 6) is unusually slow for a δ Scuti star—compare with, for example, Figure 7 in Rodríguez et al. (2007) and Figure 3 in Ulusoý et al. (2013). One possibility is that the star is in fact a binary, consisting of a δ Scuti pulsator with a luminous blue companion. The excess short-wavelength radiation contributed by the companion would then dilute the amplitude of the pulsations in the blue. However, this does not readily explain the difference between the wavelength dependence of the two primary modes.

7. Conclusions

Six of the binary stars modeled in this paper, four eclipsing systems and two reflection-effect binaries, consist of subdwarf B stars with cool secondaries. Periods lie in the range 1.8–2.3 hr. The two reflection-effect systems are among the shortest-period systems known in this class (Schaffenroth et al. 2019, 2022). Two further binaries consist of hot WD primaries with cool companions. From the light-curve fits together with fits of the SEDs and the Gaia parallaxes we tried to constrain the companions, which seem to be M dwarfs in all cases.

The remaining three stars are pulsators, two of which are very highly reddened. ATL 1843+0226 is a highly obscured ($A_V > 5$ mag) SX Phoenicis star. It is unusual for that type of object in that it is a field star, residing near the Galactic thin disk. Furthermore, it shows an unusual bump on the descending branch of its light curve. The nature of ATL 1853+0339 is unknown: the light variations are dominated by 0.110 and 0.118 day periodicities, but there is evidence of at least two further periodicities. Only one of the periodicities show the amplitude increase with decreasing wavelength, which is expected for a pulsating star.

Nine of the eleven stars lack spectroscopy; this is required to improve the modeling of these objects. Spectra could be used for more accurate SED fitting, and, in the case of binary systems, for the determination of mass ratios from radial velocity measurements. In the case of ATL 1853+0339, spectroscopy promises to be particularly interesting. First, it could be used to check the suspected high luminosity and

reddening of the star. Second, it might reveal whether ATL 1853+0339 is a binary, either through a composite spectrum, or, if a close system, through large radial velocity changes. Third, high-dispersion time-series spectroscopy could provide additional information about pulsation modes, either through small radial velocity shifts, or through line profile variations.

Allocation of telescope time by the South African Astronomical Observatory, and the smooth operation of the equipment, are acknowledged. The authors are particularly grateful for Director’s Discretionary Time awarded in order to obtain SALT spectra of ATL 1843+0226. This research has made use of the VizieR catalog access tool and the Simbad Astronomical Database at CDS, Strasbourg, France; bolometric corrections from the MESA Isochrones and Stellar Tracks; the cumulative reddening maps of Green et al. (2018);¹³ and the results of various large photometric surveys referred to in Section 6 of the paper. A.K. acknowledges support from the National Research Foundation (NRF) of South Africa and from the Ministry of Science and Higher Education of the Russian Federation grant 075-15-2022-262 (13.MNPMU.21.0003). Helpful comments from the referee led to improvements in the paper.

Data Availability

ATLAS and CSS photometry are respectively available from the Mikulski Archive for Space Telescopes at DOI:[10.17909/t9-2p3r-7651](https://doi.org/10.17909/t9-2p3r-7651) and from the Catalina Surveys Data Release 2 site.¹⁴ SAAO photometry is available from the first author.

Appendix A

Phased ATLAS and CSS Light Curves

Phase-folded light curves of the ATLAS and (where available) CSS photometry of the stars (Figure A1).

¹³ <http://argonaut.skymaps.info/>

¹⁴ <http://nesssi.cacr.caltech.edu/DataRelease/>

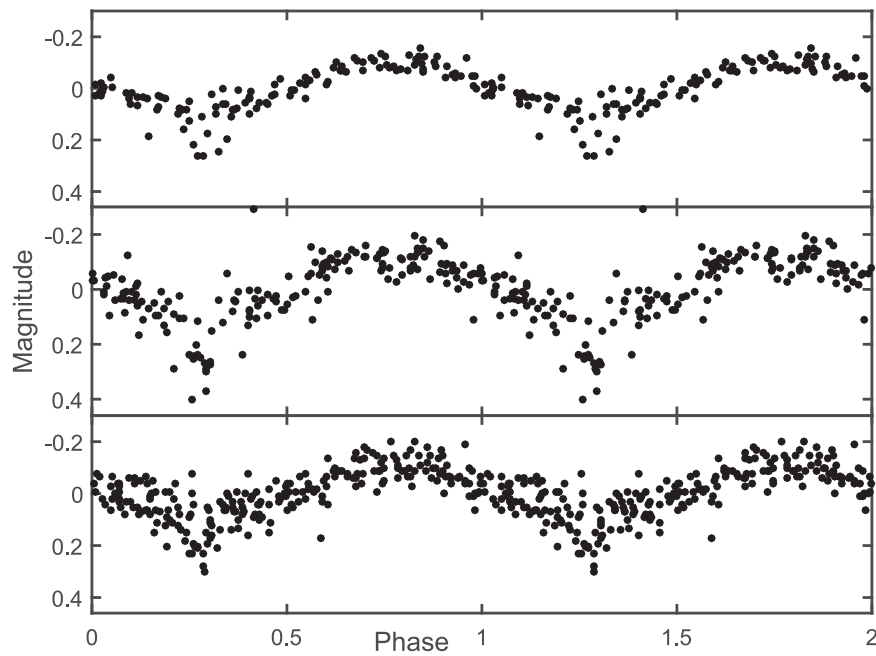


Figure A1. From top to bottom: ATLAS *c*, ATLAS *o*, and CSS photometry. The complete figure set (11 images) is available in the online journal. (The complete figure set (11 images) is available.)

Appendix B ED Fits

Plots of the SED fits for the binary stars (Figure B1).

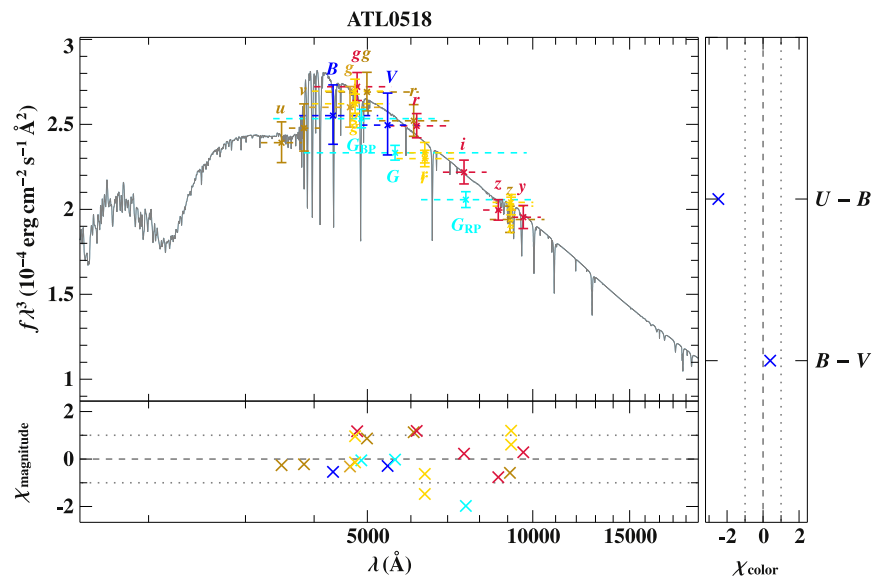


Figure B1. The color coding of the sources of the photometry is GALEX (dark violet), TD1 (dark violet), FAUST (dark violet), Johnson (blue), Geneva (crimson), Stroemgren (green), SDSS (golden), VST (golden), SkyMapper (dark golden), PS1 (crimson), Hipparcos (cyan), Tycho (brown), Gaia (cyan), BATC (gold), JPLUS (steel blue), SPLUS (steel blue), DECam (gold), DENIS (orange), 2MASS (red), UKIDSS (pink4), VISTA (red4), INT (maroon), SMASH (gold), HST (black), WISE (magenta), Spitzer (purple), SWIFT (deep pink), XMM (deep pink), and NSFCam (red4). The complete figure set (8 images) is available in the online journal.

(The complete figure set (8 images) is available.)

ORCID iDs

C. Koen  <https://orcid.org/0000-0003-2291-2660>A. Kniazev  <https://orcid.org/0000-0001-8646-0419>

References

- Balona, L. A. 2018, *MNRAS*, **479**, 183
- Baran, A. S., Østensen, R. H., Heber, U., et al. 2021, *MNRAS*, **503**, 2157
- Bellm, E. C., Kulkarni, S. R., Barlow, T., et al. 2019, *PASP*, **131**, 8002
- Bensby, T., Fletzing, S., & Oey, M. S. 2014, *A&A*, **562**, A71
- Bianchi, L., Herald, J., Efremova, B., et al. 2011, *Ap&SS*, **335**, 161
- Blake, R. M., Delaney, P., Khosravani, H., Tome, J., & Lightman, M. 2003, *PASP*, **115**, 212
- Breger, M., & Bregman, J. N. 1975, *ApJ*, **200**, 343
- Chambers, K. C., Magnier, E. A., Metcalfe, N., et al. 2016, arXiv:1612.05560
- Chen, X., Wang, S., Deng, L., et al. 2020, *ApJS*, **249**, 18
- Claret, A., & Bloemen, S. 2011, *A&A*, **529**, A75
- Coşkunoğlu, B., Ak, S., Bilir, S., et al. 2011, *MNRAS*, **412**, 1237
- Copperwheat, C. M., Marsh, T. R., Dhillon, V. S., et al. 2010, *MNRAS*, **402**, 1824
- Drake, A. J., Graham, M. J., Djorgovski, S. G., et al. 2014, *ApJS*, **213**, 9
- Edelmann, H. 2003, PhD, Friedrich-Alexander-University, Erlangen-Nürnberg
- Fitch, W. S. 1981, *ApJ*, **249**, 218
- Fitzpatrick, E. L. 1999, *PASP*, **111**, 63
- Gaia Collaboration 2021, *A&A*, **649**, A1
- Geier, S., Raddi, R., Gentile Fusillo, N. P., & Marsh, T. R. 2019, *A&A*, **621**, A38
- Gentile Fusillo, N. P., Tremblay, P.-E., Gansicke, B. T., et al. 2019, *MNRAS*, **482**, 4570
- Green, G. M., Schlafly, E. F., Finkbeiner, D., et al. 2018, *MNRAS*, **478**, 651
- Guzik, J. A. 2021, *FrASS*, **8**, 55
- Han, Z., Podsiadlowski, P., Maxted, P. F. L., & Marsh, T. R. 2003, *MNRAS*, **341**, 669
- Han, Z., Podsiadlowski, P., Maxted, P. F. L., Marsh, T. R., & Ivanova, N. 2002, *MNRAS*, **336**, 449
- Heber, U. 2016, *PASP*, **28**, 082001
- Heinze, A. N., Tonry, J. L., Denneau, L., et al. 2018, *AJ*, **156**, 241
- Henden, A. A., Levine, S., Terrell, D., & Welch, D. L. 2015, AAS Meeting, **225**, 336.16
- Hilditch, R. W., Harries, T. J., & Hill, G. 1996, *MNRAS*, **279**, 1380
- Husser, T.-O., Wende-von Berg, S., Dreizler, S., et al. 2013, *A&A*, **553**, A6
- Jeon, Y.-B., Kim, S.-L., & Nemeč, J. M. 2010, *PASP*, **122**, 17
- Johnson, D. R. H., & Soderblom, D. R. 1987, *AJ*, **93**, 864
- Jones, D., & Boffin, H. M. J. 2017, *NatAs*, **1**, 0117
- Kallrath, J., & Milone, E. F. 2009, *Eclipsing Binary Stars: Modeling and Analysis* (2nd ed.; New York: Springer)
- Kniazev, A. Y., Malkov, O. Y., Katkov, I. Y., & Berdnikov, L. N. 2020, *RAA*, **20**, 119
- Koen, C. 2019, *MNRAS*, **490**, 1283
- Koen, C. 2022, *MNRAS*, **510**, 1857
- Kovalev, M., Bergemann, M., Ting, Y.-S., & Rix, H.-W. 2019, *A&A*, **628**, A54
- Kupfer, T., Ramsay, G., Roestel, J. v., et al. 2017, *ApJ*, **851**, 28
- McNamara, D. H. 1995, *AJ*, **109**, 1751
- Muhie, T. D., Dambis, A. K., Berdnikov, L. N., Kniazev, A. Y., & Grebel, E. K. 2021, *MNRAS*, **502**, 4074
- O'Donoghue, D., Kilkeny, D., Koen, C., et al. 2013, *MNRAS*, **431**, 240
- Onken, C. A., Wolf, C., Bessell, M. S., et al. 2019, *PASA*, **36**, 33
- Østensen, R. H., Geier, S., Schaffenroth, V., et al. 2013, *A&A*, **559**, A35
- Parsons, S. G., Marsh, T. R., Copperwheat, C. M., et al. 2010, *MNRAS*, **402**, 2591
- Paxton, B., Smolec, R., Schwab, J., et al. 2019, *ApJS*, **243**, 10
- Pecaut, M. J., & Mamajek, E. E. 2013, *ApJS*, **208**, 9
- Pecaut, M. J., Mamajek, E. E., & Bubar, E. J. 2012, *ApJ*, **756**, 154
- Press, W. H., Teukolsky, S. A., Vetterling, W. T., & Flannery, B. P. 1992, *The Art of Scientific Computing* (2nd ed.; Cambridge: Cambridge Univ. Press)
- Ricker, G. R., Winn, J. N., Vanderspek, R., et al. 2015, *JATIS*, **1**, 014003
- Rodríguez, E., Fauvaud, S., Farrell, J. A., et al. 2007, *A&A*, **471**, 255
- Sadun, A. C., & Ressler, M. 1986, *PASP*, **98**, 504
- Schaffenroth, V., Casewell, S. L., Schneider, D., et al. 2021, *MNRAS*, **501**, 3847
- Schaffenroth, V., Classen, L., Nagel, K., et al. 2014, *A&A*, **570**, A70
- Schaffenroth, V., Geier, S., Heber, U., et al. 2018, *A&A*, **614**, A77
- Schaffenroth, V., Barlow, B. N., Geier, S., et al. 2019, *A&A*, **630**, A80
- Schaffenroth, V., Pelisoli, I., Barlow, B. N., et al. 2022, *A&A*, **666**, A182
- Schafly, E. F., Meisner, A. M., Stutz, A. M., et al. 2016, *ApJ*, **821**, 78
- Schechter, P. L., Mateo, M., & Saha, A. 1993, *PASP*, **105**, 1342
- Skrutskie, M. F., Cutri, R. M., Stiening, R., et al. 2006, *AJ*, **131**, 1163
- Stankov, A., & Handler, G. 2005, *ApJS*, **158**, 193
- Terrell, D., & Wilson, R. E. 2005, *Ap&SS*, **296**, 221
- Ulusoy, C., Gulmez, T., Stateva, I., et al. 2013, *MNRAS*, **428**, 3551
- Wolf, C., Onken, C. A., Luvaul, L. C., et al. 2018, *PASA*, **35**, E010
- Wright, E. L., Eisenhardt, P. R. M., Mainzer, A. K., et al. 2010, *AJ*, **140**, 1868
- Zari, E., Rix, H.-W., Frankel, N., et al. 2021, *A&A*, **650**, A112
- Ziaali, E., Bedding, T. R., Murphy, S. J., Van Reeth, T., & Hey, D. R. 2019, *MNRAS*, **486**, 4348